ADVANCED MATERIALS
www.advmat.de

Mechanical Properties of Conducting Printed Nanosheet Network Thin Films Under Uniaxial Compression

Aaron D. Sinnott, Adam Kelly, Cian Gabbett, Jose Munuera, Luke Doolan, Matthias Möbius, Stefano Ippolito, Paolo Samorì, Jonathan N. Coleman, and Graham L.W. Cross**

Thin film networks of solution processed nanosheets show remarkable promise for use in a broad range of applications including strain sensors, energy storage, printed devices, textile electronics, and more. While it is known that their electronic properties rely heavily on their morphology, little is known of their mechanical nature, a glaring omission given the effect mechanical deformation has on the morphology of porous systems and the promise of mechanical post processing for tailored properties. Here, this work employs a recent advance in thin film mechanical testing called the Layer Compression Test to perform the first in situ analysis of printed nanosheet network compression. Due to the well-defined deformation geometry of this unique test, this work is able to explore the out-of-plane elastic, plastic, and creep deformation in these systems, extracting properties of elastic modulus, plastic yield, viscoelasticity, tensile failure and sheet bending vs. slippage under both out of plane uniaxial compression and tension. This work characterizes these for a range of networks of differing porosities and sheet sizes, for low and high compression, as well as the effect of chemical cross linking. This work explores graphene and MoS_2 networks, from which the results can be extended to printed nanosheet networks as a whole.

1. Introduction

The rise of nanoscience, and in particular 2D nanomaterials, has led to the discovery of a plethora of new materials with a range of exotic and exciting properties with the potential to revolutionize current technologies. Owing to exceptional mechanical properties[1] and conductivities,[2] this new branch of materials sees application in a wide range of research and technological fields. However, the problem of large-scale fabrication remains, with methods of incorporating these nanomaterials into functional devices being one of the key areas of research required for the advancement of the field.

To this end, many techniques have been developed in order to allow the production of 2D nanomaterials en-masse, the leading of which (considering top-down approaches) are exfoliation techniques. While several exfoliation methods exist, such as Liquid Phase Exfoliation (LPE)[3] and electrochemical exfoliation,[4] they all operate under a similar principle of shearing flakes of quasi 2D material (e.g., graphene) from their bulk counterpart (e.g., graphite) in solution. Advantages of exfoliation techniques for large scale production include tunable nanosheet thicknesses and lateral sheet size, as well as the ease of production and the ability to scale the technique to very large batch sizes.[5] One of the most promising applications of the resulting solution of exfoliated flakes is in the field of printed electronics, whereby the solution is used, for instance, in a spray coating process to deposit layers of conductive nanosheets, which can form flexible electronic circuits.[6] There exists a large range of applications for such films, owing to the fact that nanosheets can be conducting (MXenes and Graphene), semiconducting (TMCs and phosphorene), or insulating (silicates and boron nitride).[7]

This tunability and scalability have made such networks the target of much research into their electrical capabilities.[8] However, their structures are poorly understood from a mechanical and morphological standpoint, a concerning gap in knowledge given that it is known that the morphology of such networks (namely the sheet alignment and porosity) has a profound influence on their electrical properties.[8,9] Knowing the capabilities and limitations of such a material is key to its adoption into useable applications, and the unique geometry and morphology of these networks means that there is very little foundational work

A. D. Sinnott, A. Kelly, C. Gabbett, J. Munuera, L. Doolan, M. Möbius, J. N. Coleman, G. L. Cross
Trinity College Dublin
CRANN
43 Pearse St, Dublin 2 D02 W085, Ireland
E-mail: colemaj@tcd.ie; crossg@tcd.ie
S. Ippolito, P. Samorì
University of Strasbourg
CNRS
ISIS UMR 7006
8 Alleé Gaspard Monge, Strasbourg F-67000, France

The ORCID identification number(s) for the author(s) of this article can be found under https://doi.org/10.1002/adma.202306954

DOI: 10.1002/adma.202306954

that can be applied to understand their mechanical properties. In this paper, we explore this gap in knowledge, and investigate the low strain mechanical response of sprayed networks of graphene nanosheets using nanomechanical indentation techniques.

Viewed as a granular system, these networks present a further challenge as their mechanical response cannot be described by that of a single phase of matter; with granular systems in general often presenting features of solids, liquids, gases, and more exotic properties.[10] Due to the small size of the grains in this case (best measured in nm), their semi-aligned nature, and strong cohesive forces, their compressive response is most reminiscent of a highly viscoelastic material, which we will show in this paper. As such we treat the compressive response here as solid in nature over application of stress in short timescales and low strains, while quantifying the viscous component of their deformation also via creep experiments. We present an analysis of the mechanical dynamics that may influence morphological changes within these films throughout nanomechanical compression. We explore also the difference in response for networks comprised of exfoliated graphene nanosheets of different sizes, as well as the effect of chemical cross-linking on the mechanical response of MoS_2 networks.

While methods for in-depth mechanical explorations of supported thin films in general are in their infancy (primarily owing to the difficulty of separating the substrate and film response during nanoindentation,[11]) sprayed nanosheet networks provide a plethora of further unique differences and challenges from established materials. The combination of a series of Vander-Waals (vdW) bonded flakes in a packed semi-aligned network represents a highly unusual cohesive granular system of nanoscale flakes about which very little is known. The closest studied analytical analogue currently is to jammed systems which are similarly highly porous, but fail to capture the nature of a system of individual flakes that experience close range attractional forces (vdW), friction, and bending, key parameters that represents significant changes in the mechanical response.

Analytical analogues to define morphology such as Philipse' random contact equation,[12] which attempts to predict the volume fraction of a jammed system of thin disks or rods in terms of their aspect ratio and average contact number, fall short due to key assumptions such as stiff disks, independent contacts, random packing, and oriental disorder, which tends to vastly underestimate the packing fraction and don't attempt to explain mechanical response with applied strain. As such, current analytical considerations are in their infancy with regards to these networks. Experimental analogues are rudimentary as well, generally limited to bulk measurements of platelet structures such as clays which fail to capture the aligned structure, low porosity, thin film nature, non-colloidal nature, and more. Similarly, gel dispersions and foams.[13] (for which nanosheet volume fraction is significantly lower), cohesive granular systems,[14] and bulk sheet folding/crumpling experiments[15] all fall short as a comparison to a fundamentally vdW dominated system of aligned nano-scale flakes and remain unexplored in the form of thin films. As such there is little to no groundwork in the field and we present in this work the first exploration into the mechanical response of such networks to out of plane mechanical compression.

2. Sample Preparation

Layer Compression Test (LCT) experiments were performed on nanosheet networks using a 55 µm diameter diamond flat punch tip (Synton). Graphene films were produced in batches via a well-established liquid phase exfoliation technique in solution of DI water and sodium cholate surfactant, and size selection via cascade centrifugation, with average flake sizes ranging from ≈300 to ≈930 nm and average sheet thickness of 8 to 41 layers measured via AFM sampling. The graphite was sourced from Asbury Carbons. These batches were deposited with a spray coating process to thicknesses in the range of 6.3 to 11.5 µm (measured using precise substrate to surface determination with the nanoindenter and verified with FIB cross sections) on glass substrates with a thin (≈50 nm) gold layer between the two (giving a substrate to film modulus ratio in the range of 1000:1, which is favorable for the LCT). Detailed morphological information of the networks has been characterized as a function of average nanosheet size as presented in **Table 1** in a separate publication.[9b]

This tip size to film thickness gives a contact aspect ratio between 4.8 and 8.7. The effect of contact aspect ratio on the results in this range is expected to be negligible.[16] This thickness range was chosen to make mechanical analysis more reliable with minimal influence from surface misalignment to the punch face and sample inhomogeneity.[17] These networks are labelled for convenience from this point on as graphene samples *I, II, III*, and *IV*, with increasing average nanosheet size from *I* through *IV*. A sample made of liquid phase exfoliated MoS_2 sheets was also explored. These parameters can be seen in full in Table 1. Morphological information of such liquid phase exfoliated nanosheets can be found in past literature.[3b,18]

In order to investigate the effect of sheet cross linking on compressive mechanics, two identical samples of the MoS_2 network were prepared from the same batch of LPE nanosheet ink. This consisted of an unprocessed control sample and an identical sibling sample processed via sulphur vacancy healing by introduction of 1,4-benzenedithiol molecules. Such cross linking has promise as a means of improving charge transport by introducing more electrical percolation pathways.[19] However, its influence on the mechanical properties of the network is unknown.

Table 1. Sheet and network parameters for networks used in this study. Networks labelled *I* through *IV* are liquid phase exfoliated graphene networks. MoS_2 networks used were also exfoliated using LPE techniques, which have a larger layer thickness than graphene. Sheet thickness and length values given are averages based on AFM measurements. Zero strain volume fraction is predicted from previous morphological studies on samples with the same preparation,[9b] and verified on Sample *I* via FIB-SEM tomography.

Sample	Sheet Thickness [layers]	Average Length [nm]	Film Thickness [µm]	Zero Strain Volume Fraction
I	8	300	6.3	0.6
II	11	340	7.9	0.58
III	20.5	640	9.7	0.54
IV	40.9	932	11.5	0.5
MoS_2	6 (18)	300	10	NA

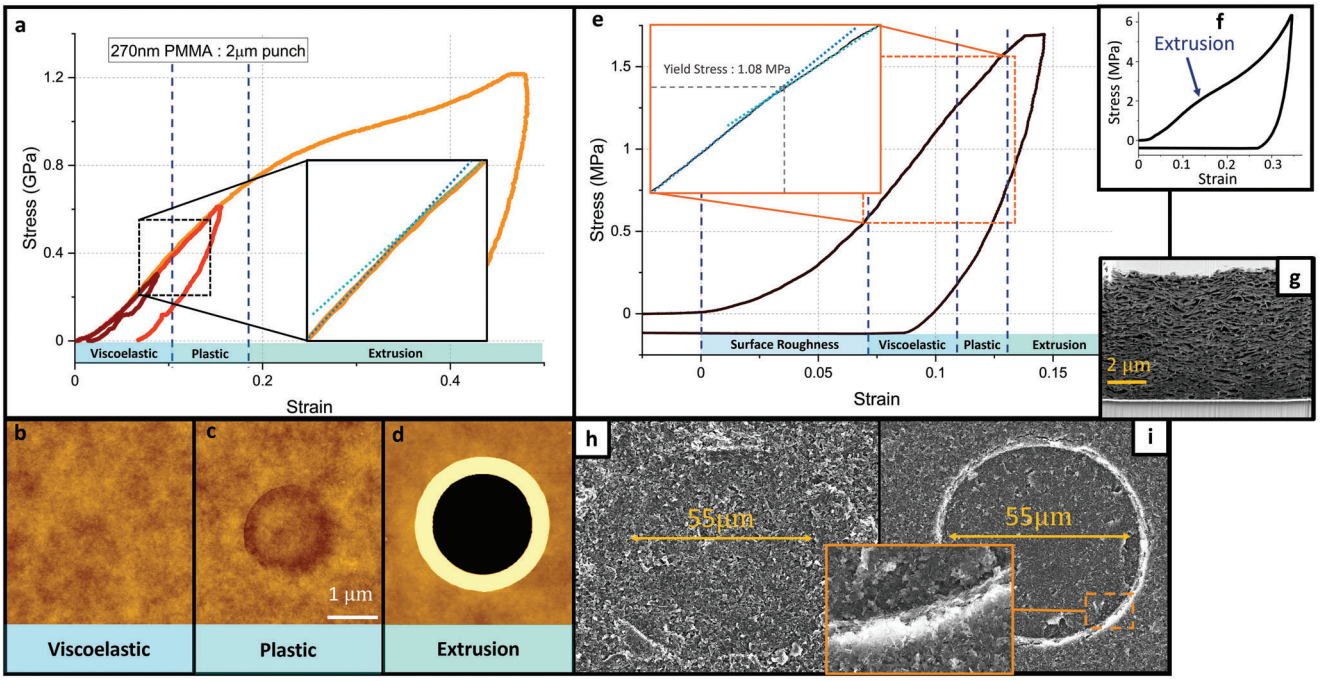

Figure 1. a) Stress vs strain curve for an LCT indent on a 270 nm thick PMMA film on a Si substrate with a 2 μm diameter flat punch tip, displaying the separation of elastic and plastic behaviour in LCT by a distinct yield kink between these two linear regions, and the confinement failure at high strain (labelled extrusion). Three indents are shown, one each with a max load in the viscoelastic, plastic, and confinement failure regimes. b–d) show AFM traces of the surface after these indents, displaying elastic and plastic behavior before and after the yield kink, and material buildup after confinement failure. e) Stress vs strain curve for an LCT indent on graphene Sample *I* with a 55 μm diameter flat punch tip, displaying the same features and regimes as on amorphous solids such as polymers, as well as a significant inflection due to surface roughness at the lowest strains, with surface roughness displayed by FIB-SEM cross section in (g). f) displays an indent on the same sample to a higher strain, better displaying the inflection caused by confinement failure. h,i), SEM images of indents on graphene networks, showing the plastic behavior for indents pre confinement failure, and the ring of built-up material after confinement failure.

Direct comparison of properties including modulus and adhesive strength can be made between the cross – linked and unprocessed samples of MoS_2 at a given strain, given that the samples are otherwise identical and share the same morphology excepting the cross linking.

3. Layer Compression Test of Polymer and Nanosheet Network Thin Films

As mentioned above, traditional nanoindentation techniques struggle to accurately examine supported thin films, and nanosheet networks present a particular set of new challenges compared to traditional hard materials like polymers, metals or ceramics; namely large amounts of surface roughness, porosity, and location to location inhomogeneity which are incompatible with traditional sharp-tipped nanoindentation techniques.[20] To this end, we use a novel indentation technique, called LCT, which allows for acute mechanical characterization of supported thin films separating regimes of elastic and inelastic deformation. In particular, the LCT can reveal a sharp yield transition between the two, with minimal and correctable influence from the substrate.[16,21]

The LCT is a recently established technique that utilizes a cylindrical flat punch tip with diameter much larger than the thickness of the film that has been well aligned to its surface utilizing a micropositioning tilt stage, allowing full tip face to sample contact after short penetration into the sample (typically <0.01 strain).[21,22] The combination of large contact aspect ratio, and the confining effect of the surrounding film on the puck compressed by the punch, limits lateral strain within the compressed puck. This, combined with a substrate several times stiffer than the supported film, approximates a state of uniaxial strain (US) within the compressed region, allowing close examination of elastic and plastic deformation properties of the film even to high strains.[16] Crucially, the LCT allows for separation of the film and substrate response provided sufficiently high substrate to film modulus is utilized.[16,21] As well as this, the LCT works to minimize some of the other hindering properties unique to nanosheet networks: the large contact area works to average out location dependent inhomogeneity within the film, and lessens the impact of surface roughness inherent to the production of printed networks.

3.1. Polymer Film LCT

To set the stage for our results on novel nanosheet networks, we first present a stress vs strain measurement of an isotropic, ductile film using our technique in **Figure 1**a. The LCT indentation was performed using a 2 μm diameter diamond flat punch on a 270 nm thick film of PMMA supported on a flat silicon wafer substrate. The film was, prepared via a standard spin coating recipe.

The stress–strain curve of a typical LCT indent on an elastic-plastic sample is defined by two linear regions separated by a distinct kink.[16,21] At low strain there is an initial linear region of elasticity, whereby all deformation is elastic in nature. For standard isotropic homogenous materials, like polymer glasses, the slope of the curve in this region is represented by the confined modulus M (see Equation (1)).

$$M = \frac{h_0}{\pi a^2} \frac{\Delta L}{\Delta h} = \frac{E(1-\nu)}{(1+\nu)(1-2\nu)} \tag{1}$$

Where h_0 is the initial film thickness, a is the punch diameter, L is the applied load, h is the current indentation depth, E is the Young's modulus, and ν is the Poisson ratio. A distinct kink is then observed as the curve linearizes to a second constant slope. This kink is the confined plastic yield point, occurring at confined yield stress Y_c, higher than the unconfined yield Y due to the confined geometry:

$$Y_c = \frac{1-\nu}{1-2\nu} Y \tag{2}$$

Occurring here at ≈0.4 GPa. Beyond this any further deformation is plastic in nature and the slope is the bulk modulus K.

$$K = E\frac{1}{3(1-2\nu)} \tag{3}$$

The degree of elastic/plastic deformation can be determined by the residual strain left following unloading of the punch, with purely elastic indents performed to a max load lower than Y_c returning to 0 strain after unload with no residual strain present Figure 1a displays three curves, one for indents to a max load below the yield slope change shown in maroon, which displays no hysteresis on unload and is indicative of a purely elastic indent. The orange curve displays an indent with a maximum load above the yield point, showing significant unload hysteresis indicative of plastic deformation. An AFM trace of the surface after the indent represented by the maroon curve is shown in Figure 1b, showing that the maroon curve was purely elastic and left no permanent deformation, and a corresponding trace for the orange curve in Figure 1c shows clear plastic deformation. More in depth exploration of this elastic-plastic transition and corresponding slope change is found in previous publications, and is a feature of uniaxial strain.[16,21]

While the relations in Equations (1)–(3) hold for isotropic elastic-plastic materials, more complex systems such as nanosheet networks that experience a degree of anisotropy require separate analysis that will be described later, even if they should exhibit similar elastic-plastic behavior. As such the confined modulus in Equation (1) will be altered to account for the anisotropy and allow for modulus measurement, and analysis of the plastic portion beyond Y_c will not be approached in this work.

The uniaxial strain approximation of the LCT holds to ≈20% strain on traditional amorphous materials such as polymers. At strains beyond this, the confining effect of the surrounding film is no longer sufficient to contain the large lateral stresses applied to it, causing the puck of material to extrude outward from under the punch into the surrounding material. This is characterized by an inflection in the stress vs strain curve, and a subsequent extremely large residual strain, as can be seen in the yellow curve in Figure 1a. This confinement failure causes a 'ring' of extruded material to build up around the edge of the indent, shown in Figure 1d

3.2. Graphene Network LCT

A typical indent on a sprayed graphene sample (Sample *I*) is shown in Figure 1e, and an indent to a higher maximum load on the same sample in Figure 1f. Unless otherwise stated, all indents on the nanosheet networks in this work were load controlled with a constant loading rate over the course of 100 s (i.e., a 5 mN max load indent has a constant loading rate of 0.05 mN s^{-1}), a 5 s holdtime at maximum load, and a 0.2 mN s^{-1} constant unload rate. The features of the stress vs strain curve are comparable to those seen in LCT results for solid polymers and other soft supported films: an initial compression with minimal lateral strain to significant penetration depth followed by escape of material as the surrounding film material fails to confine the material under the punch.[16,23] In our nanosheet samples, material extrudes outward from under the punch and a ring of extruded material becomes visible around the indent at ≈0.13 strain, the stress vs strain inflection shown in Figure 1f,i displays a resulting ring of extruded material after such a point. Extrusion is still characterized by a distinct inflection in the stress–strain curve and a subsequent ring of extruded material as is the case for other amorphous materials, indicating that extrusion still occurs in a defined event and 'leakage' into the surrounding film is low over short timescales. Load vs displacement response was repeatable location to location on samples *I* through *III* and both MoS_2 samples. Sample *IV* presented minor variability due to variable thickness from the spraying of such large sheets. This was corrected for with careful locational choice and statistical averaging.

Understanding the features present in this stress–strain curve is the first step to understanding the mechanical behavior of these films. First, in the region of zero-strain up to ≈0.06 strain (in Figure 1e) is a concave inflection. On flat, smooth surface samples such an inflection is often the result of initial incomplete punch-sample contact due to a residual misalignment between the tip face and sample surface.[24] We used a region of bare gold substrate on each sample to determine that sample misalignment corresponds to <0.01 strain only. Thus, we attribute this curved region to innate nanosheet surface roughness. While the large contact area of the punch helps to mitigate the effect of local surface roughness, variations still exist at the lowest strains due to the high degree of inherent surface roughness. SEM inspection shows average surface roughness in the range of 10% of the total thickness (Figure 1g), with modest local changes.

This causes initially low but rapidly increasing load as the effective contact area increases, only stabilizing to a near-linear rise typical of LCT indentations after this surface roughness portion has been bypassed and the tip is in full contact with the sample.[25]

The kink in this slope typical of the yield point is largely masked by this surface roughness portion for a large portion of indents. Regions with lower surface roughness show the typical features of a LCT indent on an amorphous film beyond the

initial surface roughness portion, as shown in Figure 1e. These include a linear region beyond zero strain of constant slope indicative of elastic deformation, a distinct change to a new slope at the confined yield point, a second linear region of plastic deformation, and an extrusion event where the confinement of the technique breaks down. It is at this final point the compressed puck 'extrudes' outward from under the punch into the surrounding film and a ring of extruded material becomes visible around the indent for indents performed with a max load beyond this point (Figure 1h,i) displaying indents with and without this ring for indents above and below this extrusion point). Of significant importance is the slope change ≈0.11 strain that we denote as the yield transition between viscoelastic and plastic deformation. This is consistent with that observed on amorphous materials as discussed above, and we show later in this work that this slope change does represent the point of plastic yield through analysis of the residual strain before and after this point. Following loading, we observe a mild creep behavior over 5 s hold at peak load, which is a significant feature we will discuss later. After this held peak load timeframe, the tip retracts off the surface at a constant rate of ≈0.2 mN s^{-1}. The residual strain as we cross back over zero stress during unloading represents the degree of inelastic deformation present (purely elastic processes resulting in zero residual strain). At the end of unloading, we observe a negative tensile force indicating significant adhesion between the diamond punch and compressed graphene nanosheets, which will be used for tensile measurements in a later section, and can be seen in Figure 1e.

4. Demonstrating Viscoelastic – Plastic Behaviour

While these features seem to mirror typical elastic – plastic behavior observed in amorphous solid films such as polymers, it is prudent to demonstrate such behavior directly, particularly around the slope change that we have denoted a yield point. For a system of granular vdW bonded platelets, a determinable singular yield point as in more traditional materials has not been a foregone expectation, with a more continuous plasticity mediated around weaker, more disordered flake centres being a distinct possibility.[26] We demonstrate below through analysis of residual strain above and below this slope change stress that it represents a transition from viscoelastic to plastic deformation in these networks.

Disregarding artifacts of initial incomplete punch face contact, the initial portion of LCT indentation around zero strain will be dominated by recoverable elastic or viscoelastic processes in solid materials. However, this is reliant on uniform surface contact, which is possible on flat films deposited, for instance via chemical vapor deposition or spin coating. However, on the sprayed nanosheet networks the large degree of surface roughness complicates this low strain response. The increasing contact area causes small scale local plasticity upon initial contact, as the punch interacts with and plastically deforms the local peaks before making full contact with the film at large. In low peak stress load-unload curves this results in immediate plastic hysteresis and residual strain associated with the local geometry, masking global pre-plastic processes of the full compressed puck under the punch. In regions of extensive surface roughness, the curvature from zero strain associated with surface roughness may also be extensive enough to mask the yield kink entirely.

For these reasons, in order to best display the nature of the yield transition and demonstrate the viscoelastic-plastic nature of the networks, removal of surface roughness is required. This is done by pre-patterning the region of interest with a series of initial indents at the same load in a singular location, shown in **Figure 2**a, known as a shakedown process. Such a strategy is exploited here because of several reasons: First, it removes surface roughness that would cause local surface plasticity and mask viscoelastic deformation. Second, it evolves the film to a steady state which allows for demonstration of pre and post yield behavior through successive in place indents after the shakedown, free from the effect of further strain hardening and excess sheet slippage between subsequent indents. It allows this in a single sample location which is of benefit due to inhomogeneities in surface thickness and morphology between locations. Last, it delays the onset of material extrusion to the max stress of the pre-patterning step in order to better show the plastic response post-yielding and pre-extrusion.

Though the patterning has benefits for demonstrating the low strain and yield behavior as described above, it also causes other mechanical/morphological changes such as strain hardening (evident in Figure 2a).[25] While the same constitutive features exist for unpatterned regions of the film, this no longer represents an as-received film. It is therefore important to note that the extensive pre-patterning as described here is used only to demonstrate the viscoelastic – plastic nature of the networks in this section and is not used for the determination of properties such as modulus or yield stress in later sections. Any pre-processing that is applied for determining such properties will be made clear in the relevant section.

Following the pre-patterning step, a series of incremented indents, starting with an indent at 1 mN (0.42 MPa) with subsequent indents successively increasing the peak load by 0.5 mN, was performed on the patterned location. This technique can be used to probe an elastic to inelastic transition in the LCT by determining at which peak load a discontinuity in the residual strain emerges, accompanied by a yield kink in the stress vs strain curve.[21] The stress vs strain curve for these indents is shown in Figure 2b and the corresponding residual strain for each indent is shown in Figure 2c,d for two definitions of residual strain; the point where the unload crosses zero stress, and the point where the tip detaches from the sample. Both give consistent results.

For the lowest stress indents, the network displays viscoelastic behavior. This manifests as a hysteretic unload with a constant residual strain value independent of applied stress that is non zero due to the viscous component for these indents. Creep behavior when holding the load constant is also observed, another feature of viscoelasticity which will be explored in more detail later. For indents beyond a certain critical stress, the response is observed to switch sharply from viscoelastic to plastic deformation, whereby increasing maximum stress imposed on the sample results in a steady increase in residual strain post unload, and is indicative of material yield.

The precise effective yield stress and strain of the yield transition can be determined by a visible kink in the stress strain curve that accompanies this change in residual strain response (seen at ≈0.05 strain in Figure 2b). As discussed above, this is

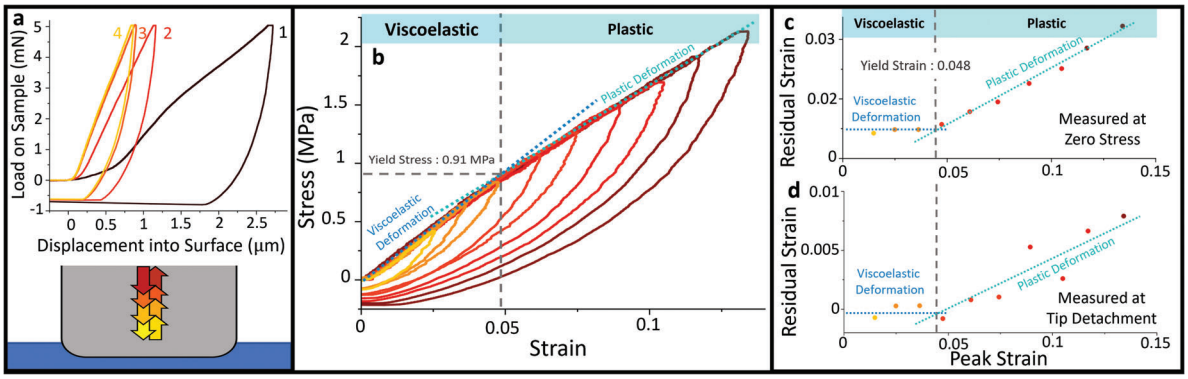

Figure 2. Demonstration of viscoelastic – plastic behavior on graphene Sample *II*. This was performed by pre patterning of the region of interest with 4 successive in place indents at a high 5 mN load (>2 MPa) to evolve the indented region to a steady state as shown in (a), the benefits of doing so are described in the text. Stress vs strain curves for successive indents at incrementally higher loads in the same location following this are shown in (b), displaying viscoelastic behavior, followed by plastic behavior. These manifest as two linear slopes separated by a yield kink. A change in residual strain behavior before and after a yield event is indicative of such a viscoelastic-plastic transition. This is shown for these indents using two definitions of residual strain; the point where we return to 0 stress after unload in (c), and where the tip detaches from the surface in (d). Both show the same change in behavior after the yield kink, indicating a viscoelastic-plastic transition.

a feature of uniaxial strain and is observed in LCT indents for amorphous elastic-plastic materials, and we can conclude that this determinable kink does represent a point of distinct inelastic yield in these films, and that the slope of the stress vs strain curve before this yield transition represents an effective viscoelastic modulus. This slope change has also been observed to be accompanied by a change in material stiffness with compression in the same manner as amorphous polymer glasses in previous publications.[25] While this indicates viscoelastic-plastic behavior as observed in amorphous solids such as polymer glasses in the LCT, we need to account for the anisotropic nature of the films before parameters such as modulus can be effectively extracted.

5. Anisotropy

While Equations (1) and (2) describe the confined modulus and yield point for amorphous films, they hold only for homogenous, isotropic materials. Networks made of 2D nanosheets, like those studied here, are subject to transverse linear isotropy, whereby the semi aligned nature of the sheets causes a difference in mechanical properties between the orthogonal in-plane directions, and the third out of plane direction in a standard cartesian coordinate system. Indentations in this work are performed in the out of plane direction (i.e., the anisotropic direction). This complicates any approach to mechanical testing, including the LCT. In the elastic regime, the stress–strain relations for an anisotropic material comprises of a matrix, accounting for material properties in the three principal directions x, y, and z, as well as in combined directions xy, xz, yz. In the case of transverse isotropy for these networks, whereby directions x and y have identical properties, the relation reduces as follows:[27]

$$\begin{bmatrix} \sigma_1 = \sigma_{xx} \\ \sigma_2 = \sigma_{yy} \\ \sigma_3 = \sigma_{zz} \\ \sigma_4 = \sigma_{yz} \\ \sigma_5 = \sigma_{xz} \\ \sigma_6 = \sigma_{xy} \end{bmatrix} = \begin{bmatrix} C_{11} & C_{12} & C_{13} & 0 & 0 & 0 \\ C_{12} & C_{22} & C_{13} & 0 & 0 & 0 \\ C_{13} & C_{13} & C_{33} & 0 & 0 & 0 \\ 0 & 0 & 0 & C_{44} & 0 & 0 \\ 0 & 0 & 0 & 0 & C_{44} & 0 \\ 0 & 0 & 0 & 0 & 0 & C_{66} \end{bmatrix} \begin{bmatrix} \varepsilon_1 \\ \varepsilon_2 \\ \varepsilon_3 \\ 2\varepsilon_4 \\ 2\varepsilon_5 \\ 2\varepsilon_6 \end{bmatrix} \tag{4}$$

As the LCT closely approximates uniaxial strain along the z direction until the point of extrusion, all strains barring ϵ_3 are approximately zero in the limit of low strain. As such this matrix reduces to

$$\begin{bmatrix} \sigma_1 \\ \sigma_2 \\ \sigma_3 \\ \sigma_4 \\ \sigma_5 \\ \sigma_6 \end{bmatrix} = \begin{bmatrix} C_{13}\epsilon_3 \\ C_{13}\epsilon_3 \\ C_{33}\epsilon_3 \\ 0 \\ 0 \\ 0 \end{bmatrix} \tag{5}$$

$$C_{13} = \frac{EE'\nu'}{(\nu - 1)\,E' + 2E(\nu')^2} \tag{6}$$

$$C_{33} = \frac{(\nu - 1)\,(E')^2}{(\nu - 1)\,E' + 2E(\nu')^2} \tag{7}$$

Where $E = E_{22} = E_{11}$ is the in-plane Young's modulus, $E' = E_{33}$ is the out of plane Young's modulus. $\nu = \nu_{12} = \nu_{21}$ is the in-plane Poisson ratio, and $\nu' = \nu_{31} = \nu_{32}$ is the out of plane Poisson ratio.

While for an isotropic material we can extract Young's modulus E and Poisson ratio ν from a single loading curve by measuring M and K through the pre and post-kink slope respectively, this is not possible for an anisotropic material like this, due to the splitting of these parameters in the anisotropic planes. Even though the stress vs strain curves appear to be similar once surface roughness is accounted for, the term C_{33} is the slope of the stress vs strain curve in elastic compression for this anisotropic case, as opposed to that presented in Equation (1). It remains beyond the capabilities of current mechanical testing techniques to accurately determine both the in and out of plane Poisson ratios and Young's moduli needed to characterize C_{33} in a thin film material. In the absence of a means of direct measurement of these parameters, we observe that the deviator term in this expression is the denominator term $2E(\nu')^2$, whereby as this approaches zero, the expression in Equation (7) approaches the out of plane Youngs' modulus E'. While ν' is not measured in

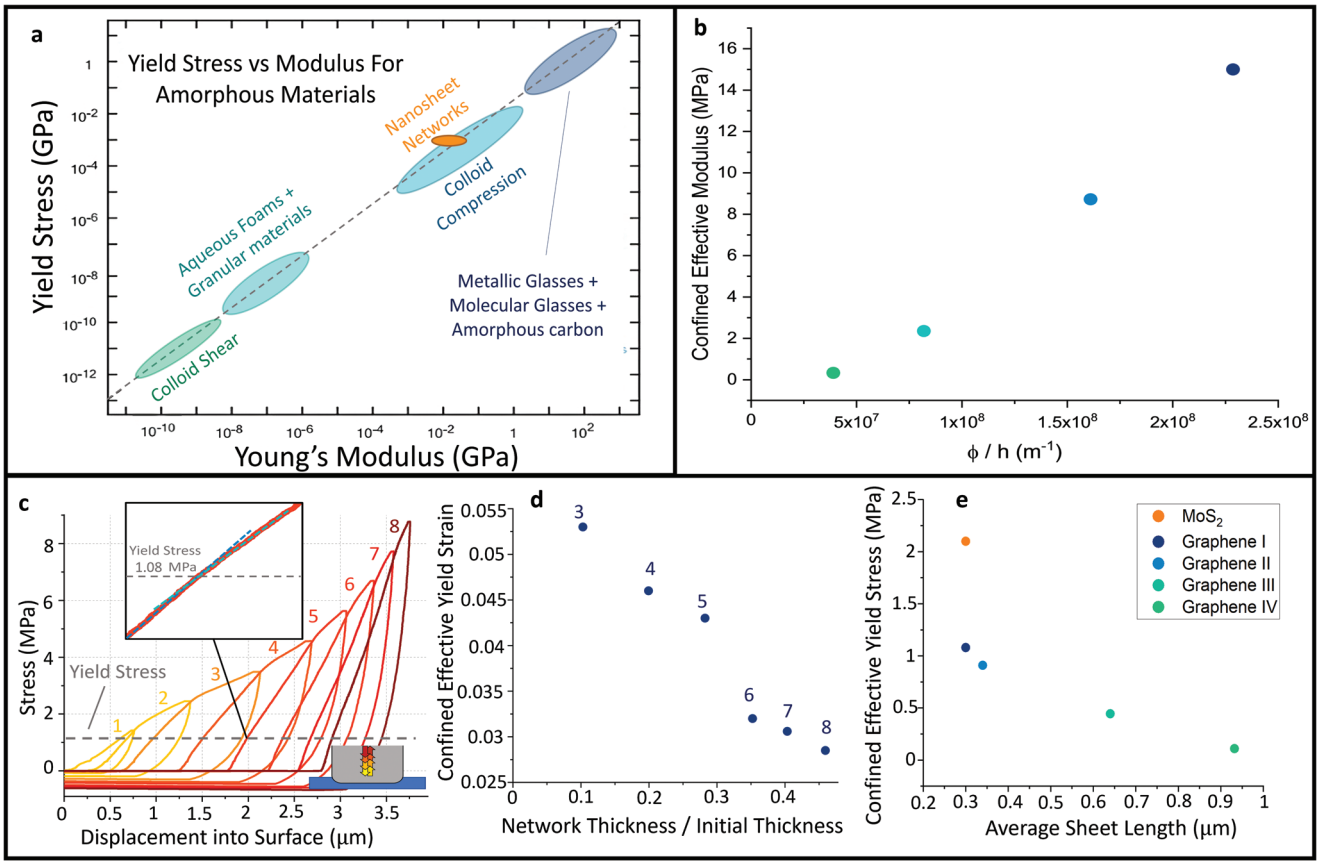

Figure 3. a) An Ashby chart of Elastic Modulus vs Yield point for amorphous materials demonstrates the universal relationship between these quantities in amorphous solids and the position of all tested nanosheet networks being in line with amorphous materials (data adapted from[41]). b) Comparison between the effective modulus of graphene nanosheet networks as a function of volume fraction and sheet thickness as per Equation (11). This relation may fail at low and high volume fractions for reasons outlined in the text. c) A series of increasing load indents on Sample *I* performed in place to probe the yield point and modulus as a function of compression while avoiding the effects of surface roughness and sample inhomogeneity. While the yield stress remains constant as the film is compressed (1.08 MPa), the yield strain for these indents reduces rapidly, as plotted in (d). The yield stress for the range of samples as a function of sheet length is plotted in (e).

this work, there are expectations on its value based on closest analogues. Materials with high porosity tend to have low Poisson's ratios,[28] with materials with more elliptical pores (as in this material) being lower again than for circular pores.[29] Closest experimental comparison can be found with semi aligned clay/shale stackings, which share in the semi aligned sheet network nature with the same anisotropic condition. For these, it is found that $E \approx 0.5\ E'$ (depending on alignment) and ν' is low in the regime of alignment interest for this work.[30] With these as reference, we may expect the deviator term to be small compared to the other terms due to its squared power scaling, resulting in a measured effective modulus from a stress–strain slope being within an acceptable range of the true Young's modulus (≤15% deviation using conservative values from geomechanical systems.[30])

In support of this is the relationship between measured modulus and yield point in this work, shown in **Figure 3**a, which displays an Ashby chart of the universal relation between Young's modulus and yield point for amorphous solids. The position of our measurements (E′ and yield stress) of nanosheet networks on this chart supports the measurements being within a reasonable range of Young's modulus, as it lies along the relation known for amorphous solids.

Considering the large degree of variance within such sprayed structures due to spraying differences, sheet size selection, drying effects, and location differences due to inhomogeneity, we assume variance between two films prepared under similar conditions is of equal or greater consideration as that given by this approximation[8] (for comparison, even well studied amorphous materials vary in Young's modulus considerably depending on sample history and preparation, for example Polystyrene, for which literature values range between 2.4 and 3.4 GPa).[31] As such we can consider our measurement of an effective contact modulus as a reasonable approximation of the out of plane Young's modulus (E'), while the authors accept that accurate measurement of the out of plane Poisson's ratio is needed for more prudent analysis of specific films.

6. Modulus Measurements

The presence of a yield point, along with the constant residual strain in indents before this point, are indicative of a

viscoelastic response in low strain indentation. As discussed above, this represents an effective confined modulus that is likely to be within a reasonable estimate of the out of plane Young's modulus, E' (Equation (7)). The residual strain present in the viscoelastic regime we attribute to sheet sliding (a dissipative process), and the recoverable elastic portion of this regime we attribute to an amalgamated sheet bending processes within the compressed region.

The modulus is measured directly from the pre kink slope of an indent on an un-patterned film in the case of a sample with sufficiently low surface roughness for this to be measured (for example the stress vs strain curve in Figure 1e). For networks of much larger sheets such as Sample *IV*, surface roughness is higher and modulus cannot be measured from a single indent on un-patterned film. In this case a single pre-patterning indent to remove the surface roughness is performed beforehand (typically < 0.1 strain). This light single indent pre patterning contrasts with the heavier shakedown process used to demonstrate viscoelastic – plastic behavior and represents only minor correctable morphological changes to the network. Pressure dependent studies on such networks have revealed that stiffness increases as the network is compressed,[25] and as such the strain at which the modulus is measured, as well as any light single indent pre patterning required, must be accounted for (for example in Figure 1e the strain would be measured only after the surface roughness inflection at ≈0.7 strain). This is done by considering the change in porosity with compression and is described further later in this section.

The measured compressive modulus E' of the graphene networks is in the range of 0.3 to 15 MPa for the graphene films *I* through *IV* explored in this work, with networks of larger sheets displaying lower moduli. As such, factors like porosity and sheet size play a large role in the modulus of the networks.

We can explore how the modulus is affected by network parameters by considering the associated mode of compression. In thin sheets, the energy expenditure to create a ridge is substantially higher than for vertices or smooth bends.[32] Assuming the majority of recoverable compression manifests from sheet bending (as sliding mechanisms constitute a dissipative process), and that most of the energy of bending sheets is expended in ridge creation, the work in bending a thin sheet is given by:[33]

$$W \approx \kappa N \left(\frac{\chi}{h}\right)^{\frac{1}{3}} \tag{8}$$

Where κ is the bending stiffness of the sheets, N is the number of folds, χ is the length of the folding ridge, and h is the sheet thickness. For our nanosheets the ridge length is equal to the sheet length; $\chi = l$. As our consideration will be volumetric, and that the nanosheets are likely to form only a single ridge each, owing to their size and aspect ratio, we can take $N = 1$. The bending stiffness of graphene sheets scales with the sheet thickness as a function of the bending angle. For small bending angles the scaling is in the range of $\kappa \propto h^2$.[34] Though this scaling will change as the networks are compressed (and therefore the bending angle changes), it is a reasonable estimate for low strain compression. The pressure to bend a sheet will depend on the work divided by the compressed volume and will be directly related to the modulus E' of the network based on the strain contribution of each fold to the network compression:

$$P \propto E' \propto W/V \tag{9}$$

As we considered this for $N = 1$, we consider the volume occupied by each nanosheet, which depends on the sheet length l, thickness h, and nanosheet volume fraction ϕ as follows:

$$V = \frac{l^2 h}{\phi} \tag{10}$$

For liquid phase exfoliated sheets, the average length of sheets scales with the thickness, so we can approximate for simplicity:[35] $l \propto h$, and combining Equations (8–10) with these considerations, it gives:

$$E' \approx \alpha \frac{\phi}{h} \tag{11}$$

where α is a constant of proportionality that will depend on the nanosheets. For example, liquid phase exfoliated sheets of graphene will share a comparable α if prepared similarly, but networks of different materials (with different bending stiffness scaling) or exfoliation techniques will have a different scaling constant. This constant captures several relations, including the scaling constant between κ and h, that from P to fold a single sheet to E' for the network, l to h, and other proportionalities.

The liquid phase exfoliated graphene networks $I - IV$ have known zero strain porosities[9b] and as such we can plot the measured modulus vs ϕ/h for these networks. The influence of surface roughness inflections, and any required light prepatterning to remove it, can be accounted for here by considering an equivalent change in ϕ with strain for the corresponding measured E'. This relation is shown in Figure 3b. The relation is appreciably linear as predicted, with small offsets likely due to subtle differences in bending angle (and therefore bending stiffness) between networks of different porosities and sheet thicknesses, or by smaller energy considerations for bowing of sheets separate from the ridge formation approximation in Equation (8). Should an analytical relation between these parameters be found we could likely improve the fidelity of these results.

Our relation holds in the range of porosities and sheet thicknesses measured here (volume fraction ≈0.5 to ≈0.64, with zero strain volume fraction given in Table 1 for each graphene sample), but may break down in more extreme regimes. For example, a regime of low porosity may limit sheet bending, as would a network of very low aspect ratio sheets, or for very thick sheets that a folding ridge model may not accurately represent. While a regime of sufficiently high porosity approaches a material more closely resembling a foam or net system, though some similarities may remain. For example, recently studied low ϕ colloidal graphene sheets attribute compressive response beyond the gelation point to a similar bending/crumpling mechanism, though with a different scaling with ϕ.[36] Therefore, while this linear relation holds within this range, more considerations may have to

be made for networks with parameters sufficiently outside the explored range.

6.1. Effect of Compression on Modulus

It is known that reducing porosity has an effect on the stiffness of these networks,[25] and the relation derived here in Equation (11) demonstrates the same. Cycled indentation testing can explore the effect of increased compression on the modulus. This can be realized by performing a series of indentations with successively higher peak stress at a single location of the film. Each indent produces a stress–strain curve with a measurable yield point and pre-kink slope, and also compresses the film such that the porosity is decreased for the next indent in the series. As we cannot account directly for the degree of material extrusion after confinement failure, the modulus measured at high compressions cannot be matched directly to a porosity, but serves as a basis for the degree of modulus increase with compression in the MPa range.

A series of such indents on graphene Sample *I* is shown in Figure 3c, revealing that the modulus in a given network increases greatly with compression, from 15 MPa with no compression to 40 MPa for the most compressed portion of the network, with values of up to 78 MPa found for more extreme compressions in the range of 30 MPa. This reveals a strong dependence on modulus with compression and porosity. Pressure dependent stiffening and densification of amorphous thin films and nanosheet networks have been reported recently in the literature,[25] and morphological changes that influence the increase in network stiffness will be explored in a future publication. Networks of MoS_2 sheets exhibit higher moduli compared to graphene of comparable sheet length, owing to the much larger bending stiffness of the flakes (≈5–11× higher for monolayer MoS_2 compared to graphene).[34,37] The MoS_2 sample ranged in modulus from 36.75 MPa to 107 MPa depending on the degree of compression.

7. Yield Point Measurement

The specifications of material yield have distinct implications for device manufacturing, being fundamental to the mechanical tolerances of a given device. Understanding the mechanisms of such yielding can allow for both greater understanding of the deformation pathways fundamental to the material class as a whole, and with further implications for post processing parameters in mass-scale device manufacture, such as roll-to-roll processing.[38] Both the stress and strain at which yield occurs, as well as how this evolves with densification, are important considerations and are explored here for these networks.

Incremented indentation testing is used to explore the effect of porosity on the yield point. The increment set on Sample *I* shown in Figure 3c shows 8 successive indents on the same sample location with successively increasing loads, each densifying the network further. They reveal that the yield stress in a given network does not change with reduction in network porosity induced by compression (as the slope change on loading denoting the yield stress does not change between the curves, as demonstrated by the horizontal dashed line in Figure 3c). As such we can conclude that the yield stress is largely independent of the network porosity (at least in the range of porosities explored here, ranging from ≈0.4 to ≈0.2 during this incremented compression on Sample *I*), or only weakly dependent upon it, and is instead governed more strongly by the properties of the individual flakes. This implies the onset of inelastic deformation is governed by local sheet deformations such as local folds, as opposed to sliding which would be more influenced by porosity and free volume that would be required to facilitate these processes. This reliance on local mechanisms is supported by examination of covalently cross – linked MoS_2, discussed in a later section.

Although the effective yield stress is independent of network compression, the effective yield strain is not. Figure 3d shows the effective yield strain for the same set of indents, defined relative to the new film thickness after each indent, with a decreasing yield strain for more highly compressed networks. As the yield stress was unaltered by the compression, it is unlikely this is due to strain hardening, and is instead likely intrinsic to the change in network parameters such as porosity, nanosheet alignment, or sheet morphology (for example, pre compressed networks already having folds present in the sheets which may reach a yielding strain at lower additional deflection than unfolded sheets). While this has not been measured as a function of these parameters (due to extrusion making this immeasurable during indentation for indents at this high strain, and any elastic recovery making post – indent analysis unreliable to extract these properties), it is evident that the yield strain reduces rapidly as the film is compressed and porosity is reduced.

The effect of sheet size on the yield stress is plotted in Figure 3e and reveals that the yield stress reduces with increasing sheet size. While it may be surprising that networks comprised of larger, thicker sheets yield at lower stresses than those of thinner sheets, it is important to consider that thicker sheets are longer, and the network pore size is also increased.[9b] This allows more space for sheet deformation, and it increases the length between individual bending moments and their fulcrum (both being located at contact points between sheets) which may reduce the overall network stiffness. This is supported by the fact that the MoS_2 sample has a measured effective yield point of 2.1 MPa, significantly higher than graphene Sample *I* which has a comparable sheet length and an effective yield point of 1.08 MPa, owing to the increased stiffness of MoS_2 sheets compared to graphene,[34,37,39] showing that stiffer sheets form networks with higher yield points when nanosheet length is accounted for. It also shows that nanosheet length has a higher influence on the yield point than sheet thickness for otherwise comparable networks.

As an aside, the role of shear in the onset of plasticity in these networks should be mentioned, as it is fundamental to the onset of plastic yield in solid materials.[40] The LCT is fundamentally an approximation of a uniaxial strain geometry and as such lowers the ratio of shear to hydrostatic pressure compared to unconfined geometries or shear-based loading. The porous and granular nature of these samples is likely to readily facilitate lateral sheet movement as a means of plastic deformation in the event of a large amount of shear injection in the network.[26] This build-up of shear and the resulting large scale lateral movements of

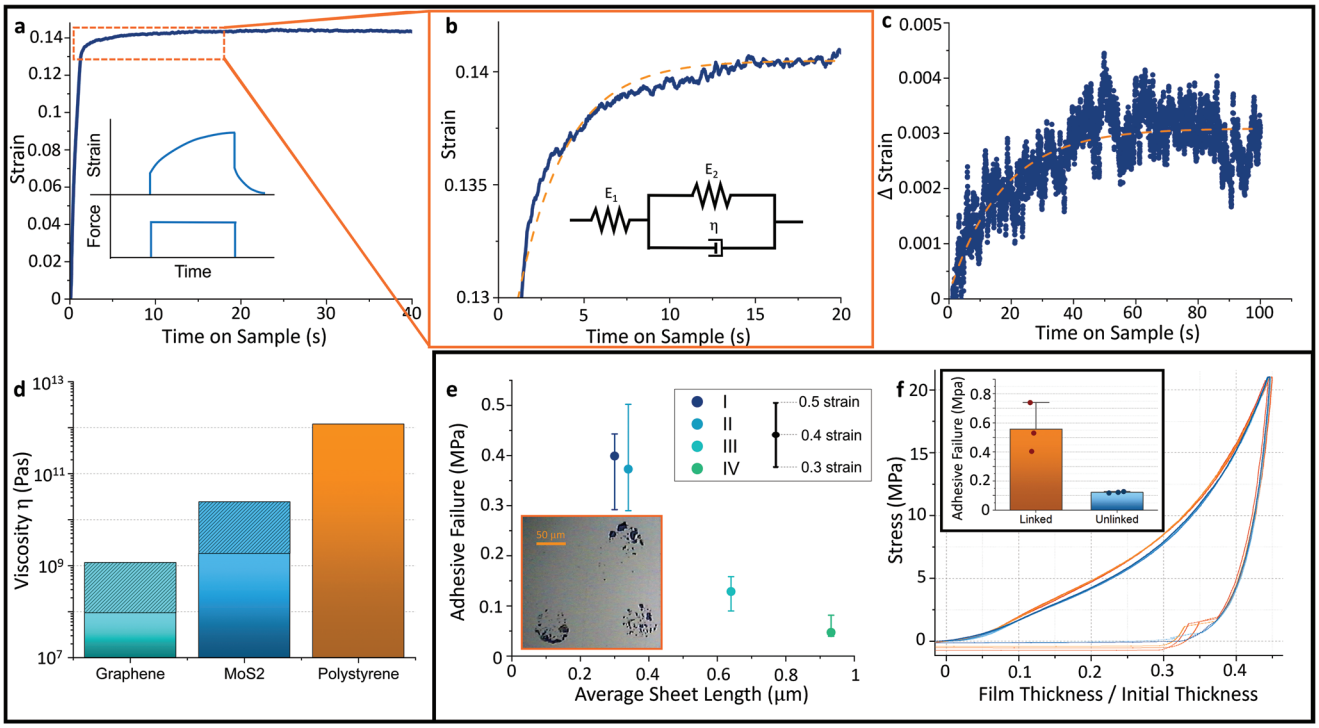

Figure 4. a) Strain vs time for a creep test at 1.5 MPa loaded over 1 s and held for 100 s on graphene Sample *II*. b) Zoomed in section of interest. Orange dotted lined shows fitting for the viscoelastic model used to extract η. The model is shown in insets in (a) and (b). The same creep test was performed on a 5 μm thick 1 000 00 Mw PS film on a Si substrate as a means of comparison, shown in (c) after a substrate correction step to remove the deformation of the Si substrate. Extracted viscosities for graphene and MoS_2 networks alongside the polystyrene film are shown in (d). Hatched regions represent the range of values for varying parameters (for graphene: compression and sheet size, for MoS_2 : compression and cross – linking). e) shows tensile stress to overcome inter-flake adhesion for each of the graphene networks studied. Error bars represent the increasing stress required for compressions ranging from 0.3 to 0.5 strain, indicative of a porosity/alignment dependence on the out of plane tensile strength of the networks, as well as a sheet size dependence. Inset shows transfer of graphene from indenter tip to gold after indentation, revealing the degree of flake coverage on the tip post indentation, even after 3 consecutive transfers. This reveals that at sufficiently high indent depths, separation occurs between flakes and not between tip and flake, and so network tensile failure is measured. f) shows stress–strain curves for otherwise identical networks of cross – linked and pristine MoS_2, and an inset showing the difference in out of plane adhesive failure for each.

the network are observed also in our geometry upon failure of the confining influence of the surrounding film at high pressures, which sees mass ejection of the confined material into the surrounding film jacket. While we attribute yield and viscoelasticity to sheet bending processes in this confined uniaxial compression, other loading geometries may facilitate lateral motions more readily via increased shear, and therefore alter the mechanical response.

8. Viscosity Measurements

As discussed above, a dissipative component to the deformation is present in these networks. This is unsurprising given that amorphous solids can experience viscoelasticity.[42] As well as this, granular materials can deform as liquids when under stress,[10a] although the degree of the response depends on the material and on factors such as grain size, shape, stress rate, cohesive forces, and many more.[14,43] Figure 2b shows stress vs strain curves of a graphene nanosheet network exhibiting hysteresis in the pre-yield portion of the curve, a feature of viscoelastic materials. As well as this, the nanosheet networks also experience a noticeable creep response when load is held constant, as shown in **Figure 4**a, which shows the evolution of punch displacement at a held constant 1 MPa stress on graphene Sample *II*. Both features are indicative of an appreciable viscous response to the deformation. This can be visualized as a slippage or sliding of sheets past one another, either as a bulk motion or individual sheet slippage into void space. This is in contrast to deformation via sheet bending which would constitute a solid response.[33]

To define the viscous component of the deformation, we leverage the uniform stress–strain state imposed by the LCT[16] and comparison to a viscoelastic model. One of the simplest viscoelastic models that adequately describes creep behavior is the standard linear viscoelastic model which models material using two springs and a dashpot. We consider here the Kelvin representation of this Zener model, as in Figure 4b. Upon application of instantaneous stress, the material instantly deforms to a constant displacement defined by E_1 and creeps toward a constant value defined by the spring E_2 in parallel with the dissipative dashpot with viscosity η. The strain response is typically expressed as follows:[44]

$$\varepsilon\ (t) = \sigma_0 \left[\frac{1}{E_1} e^{-t\left(\frac{E_2}{\eta}\right)} + \frac{E_1 + E_2}{E_1 E_2} \left(1 - e^{-t\left(\frac{E_2}{\eta}\right)} \right) \right] \quad (12)$$

where ϵ is strain and t is time after application of stress σ_0. E_1 is the spring constant of the first spring, in series with a spring and dashpot in parallel defined by E_2 and viscosity η. We can rearrange this to:

$$\varepsilon\ (t) = \sigma_0 \frac{E_1 + E_2}{E_1 E_2} - \frac{\sigma_0}{E_2} e^{-t\left(\frac{E_2}{\eta}\right)} \tag{13}$$

where the first term describes the total displacement with an offset for the creep response defined by the exponential term.

By applying a known stress over a very short timescale (≈1 s) and fitting the resulting creep behavior to the exponential term in Equation (13) we can extract a value for the viscosity of high viscosity thin films. Performing this with a 55 µm diameter flat punch tip on a 5 µm thick Polystyrene (PS) thin film (1 000 000 Mw, 21 °C) on a silicon substrate (with a substrate correction performed as standard for LCT indents[16,21]) gives a value of $\eta = 1.2 \times 10^{12}$ Pa·s, which is within expected values for glassy polymers. This may be used as a point of comparison between nanosheet thin films and viscoelastic solids.

As we attribute creep response in the nanosheet networks with dissipative flow of sheets, the process should be limited by the available void space and friction between sheets. As such, creep should depend on parameters such as sample porosity and sheet alignment. It may also be facilitated by the recovery of folded sheets, which under compression would apply stress to nearest neighbors and facilitate further dissipative deformation,[45] where stiffness may also be expected to play a role. These measurements were performed on graphene network Sample *II* as well as the MoS_2 samples. While the exact value of viscosity depends on the method of measurement and applied strain (e.g., shear vs creep experiments), wide order of magnitude comparisons to other materials can be made.

Low strain viscosity (measured at 0.42 MPa) for graphene network Sample *II* was measured to be 9.5×10^7 Pa s, over four orders of magnitude lower than the measured polystyrene film (1.2×10^{12} Pa s), and several orders of magnitude below typical viscoelastic solids.[46] This value is also several orders of magnitude higher than is typical for cohesive granular systems,[43a] and measured materials that occupy viscosities in the range of 10^8 Pa s tend to be highly thermally dependent such as polymer melts or petroleum based polymers such as pitch.[47] Large thermal variation is not expected in these nanosheet networks owing to their granular, non-molecular nature that is arrested by vdW interactions (vdW binding energy $\approx 10^{-14}$ J vs $k_B T \approx 10^{-21}$ J[48]). This is also higher than graphene polymer nanocomposites, that have been shown to increase viscosity with higher graphene content and have viscosities in the order of 10^6 Pa s.[49]

While MoS_2 shows reduced flake: flake cohesion than graphene counterparts (demonstrated in the tensile testing section), the MoS_2 network shows a viscosity of 2.16×10^9 Pa s at 0.42 MPa, over an order of magnitude higher than a graphene network of comparable sheet lengths, likely owing to the larger sheet thickness making sheet flow more difficult. This may demonstrate a greater reliance on sheet size, stiffness, and network morphology than inter-sheet interaction in the viscosity of the networks. While porosity differences may account for some of this, it is a smaller effect than that of sheet parameters (adhesion, sheet size etc). This is supported by higher strain viscosity measurements on the graphene samples. The viscosity of Sample *II* increased from 9.5×10^7 Pa s when measured at a held 0.42 MPa to 1.08×10^9 Pa s when measured at 3.37 MPa, displaying a ≈11× increase of viscosity with a large reduction in porosity in this range. This change in porosity is much larger than that between Sample *II* and the MoS_2 sample at 0.42 MPa, which displayed a ≈23× higher viscosity, displaying that factors other than porosity have a large influence on the creep response.

The viscosity of the graphene network Samples *II, III*, and *IV* measured at 0.42 MPa were 9.5×10^7, 1.35×10^8, and 1.97×10^8 Pa s respectively, showing viscosity to increase with nanosheet size despite also increasing zero strain porosities.[9b] Careful analysis of viscosity vs porosity for the networks is unavailable in absence of a means of in situ porosity measurements at high strains. Post compression porosities may be measured using FIB – SEM tomography,[9b,25] however any strain recovery, elastic or inelastic, would interfere with such measurements and make the results unreliable.

9. Tensile Testing

At the end of unloading in a standard indent as in Figure 1e,f, we observe a negative tensile force indicative of significant adhesion between the diamond punch and compressed graphene nanosheets, manifesting as a negative stress after unloading in contrast to a return to 0 stress for zero adhesive force. The measured adhesive force increases with the maximum load applied by an indent. This increase is likely due to a reducing porosity increasing the contact area between sheets. For very high peak loads this adhesion can overcome internal film cohesion. Removal of a layer of flakes from the surface was confirmed by contacting a gold substrate after the LCT and observing material transfer as redeposit of nanosheet tip contamination, owing to the adhesion energy between graphene/MoS_2 and gold/diamond compared to inter-flake cohesion.[50] The inset of Figure 4e shows significant flake deposition onto the substrate even with three successive depositions after indentation on a graphene network. The extent of the transferred flakes after high-load indentation reveals that the primary separation on unload must occur via inter-flake separation. We exploit this pull-off force as a comparative measurement of out-of-plane cohesive tensile strength of the network after high peak strain indentation. We also use this to explore the change in tensile strength imposed by cross linking of MoS_2 sheets, and how altering sheet size affects the out of plane tensile strength of the networks.

Comprehensive analysis of cohesive strength with porosity would require an in situ means of porosity analysis. In absence of this, we can display dependence on sheet size by representing a spread of values around compressions of a given strain range. This value is shown to be dependent on both material and sheet size, with networks of smaller sheets showing larger cohesion. Cohesive failure for Samples *I* through *IV* after indents with maximum strain between 0.3 and 0.5 are shown in Figure 4e. This is attributed to greater available surface area for smaller sheets, as well as less severe surface roughness for smaller liquid phase exfoliated sheets allowing larger contact areas between sheets. The MoS_2 network exhibits a much lower cohesive strength than equivalent graphene Sample *II* (0.12 vs 0.44 MPa at an indent strain of 0.45).

10. Cross Linked MoS_2

As discussed above, two identical samples of MoS_2 were produced from the same ink and spraying parameters, with one undergoing chemical cross linking via sulphur vacancy healing by using 1,4-benzenedithiol molecules.[19] This allows the effects of chemical cross linking (CL) on the compressive mechanical properties of the network to be explored. The large contact area uniaxial compression serves to explore a macro level effect of this cross linking process on the network's mechanical properties. The results are as follows in comparison to the unlinked MoS_2 sample: CL did not noticeably alter the compressive modulus or the compressive yield stress or strain of the sample. In contrast, it increased the measured creep viscosity >2× at a held stress of 0.42 MPa, from 2.2×10^9 to 4.8×10^9 Pa s. It also increased the stress required to reach extrusion by ≈25% (evident in Figure 4f), and increased the cohesive strength of the sample, increasing the stress required to reach out of plane tensile failure 5× (evident in the inset of Figure 4f).

This reveals that cross linking has little influence on the uniaxial compressive properties of the networks, but noticeably inhibits long range movement between flakes such as during creep, tensile strength, and resistance to the extrusion process. It therefore adds credence to the supposition that low strain compressive effects such as the viscoelastic response and yield are determined by short range processes such as sheet bending and folding, as opposed to longer ranged sliding processes. Altering the degree of cross linking in a sample may therefore allow for a degree of tunability in lateral and tensile stability with little change to compressive stiffnesses, which may have implications for strain sensing applications.

11. Conclusion

The out of plane mechanical properties of spray coated nanosheet network thin films were investigated via large contact area nanoindentation. A viscoelastic response was discovered, with the resulting effective elastic modulus characterized. For networks of liquid phase exfoliated graphene sheets, compressive moduli were in the region of 0.3 to 78 MPa depending on sheet size and network porosity. MoS_2 networks were found to have moduli over 2× higher than graphene networks of comparable average sheet lengths and porosity, owing to increased bending stiffness of the flakes. Networks comprised of graphene sheets with average lengths ranging from 300 to 932 nm were compared to a folding sheet model in the range of volume fractions from $\phi = 0.54$ to 0.64 which is typical of sprayed networks, finding favourable comparison to the model predicting modulus directly proportional to volume fraction and inversely proportional to sheet thickness in this range.

A yield transition to plastic deformation was characterized, with the yield stress being dependent on sheet size but independent of porosity, with networks of smaller sheets exhibiting higher yield stresses. Yield strain on the other hand was found to be reliant on porosity. The relationship between yield stress and elastic modulus was found to be consistent with other amorphous solids, and yield stress was higher for MoS_2 networks than for comparable graphene networks.

Creep behavior attributed to sheet rearrangement within the networks was fit to a standard linear viscoelastic model and compared to a polystyrene film of comparable thickness as a means of comparison with known viscoelastic solids. Extracted viscosity was over four orders of magnitude lower for graphene networks than for the polystyrene, and over three orders of magnitude lower than polystyrene for the MoS_2 network. Both networks increased by an order of magnitude with significant compression, displaying a strong dependence on porosity.

Out of plane tensile failure of the networks was tested via adhesion to the large contact area indenter tip and subsequent tension testing until failure. Tensile failure was found to occur at higher stresses for graphene networks of smaller sheets, and was dependent on porosity. The MoS_2 network exhibited tensile failure at lower stresses than for comparable graphene networks. Chemical cross linking of MoS_2 was found to increase network resistance to lateral motion, but did not alter the compressive modulus or yield stress–strain, demonstrating that these properties are largely determined by the elastic properties of the flakes rather than the interaction between them. Cross linking was associated with a 5× increase in out of plane tensile failure and a 2× increase in viscosity compared to a pristine MoS_2 network.

Acknowledgements

This publication has emanated from research conducted with the financial support of Science Foundation Ireland under Grant number [15821]. We acknowledge funding from the European Comission through the ERC projects SUPRA2DMAT (GA-833707) and FUTURE-PRINT (GA-694101) and the Graphene Flagship Core 3 project (GA-881603)

Open access funding provided by IReL.

Conflict of Interest

The authors declare no conflict of interest.

Data Availability Statement

The data that support the findings of this study are available from the corresponding author upon reasonable request.

Keywords

layer compression test, nanoindentation, nanomechanics, nanosheets, printed electronics, thin films

Received: July 14, 2023
Revised: September 17, 2023
Published online: December 14, 2023

[1] a) C. Soldano, A. Mahmood, E. Dujardin, *Carbon* **2010**, *48*, 2127; b) W. D. Nix, *Metall. Trans. A* **1989**, *20*, 2217.
[2] M. D. Hideo Aoki, *Physics of Graphene*, Springer Science & Business Media, Berlin, Germany, **2013**.
[3] a) Y. Hernandez, V. Nicolosi, M. Lotya, F. M. Blighe, Z. Sun, S. De, I. T. McGovern, B. Holland, M. Byrne, Y. K. Gun'Ko, J. J. Boland, P.

Niraj, G. Duesberg, S. Krishnamurthy, R. Goodhue, J. Hutchison, V. Scardaci, A. C. Ferrari, J. N. Coleman, *Nat. Nanotechnol.* **2008**, *3*, 563; b) J. N. Coleman, M. Lotya, A. O'Neill, S. D. Bergin, P. J. King, U. Khan, K. Young, A. Gaucher, S. De, R. J. Smith, I. V. Shvets, S. K. Arora, G. Stanton, H.-Y. Kim, K. Lee, G. T. Kim, G. S. Duesberg, T. Hallam, J. J. Boland, J. J. Wang, J. F. Donegan, J. C. Grunlan, G. Moriarty, A. Shmeliov, R. J. Nicholls, J. M. Perkins, E. M. Grieveson, K. Theuwissen, D. W. McComb, P. D. Nellist, et al., *Science* **2011**, *331*, 568.

[4] C.-Y. Su, A.-Y. Lu, Y. Xu, F.-R. Chen, A. N. Khlobystov, L.-J. Li, *ACS Nano* **2011**, *5*, 2332.

[5] K. R. Paton, E. Varrla, C. Backes, R. J. Smith, U. Khan, A. O'Neill, C. Boland, M. Lotya, O. M. Istrate, P. King, T. Higgins, S. Barwich, P. May, P. Puczkarski, I. Ahmed, M. Moebius, H. Pettersson, E. Long, J. Coelho, S. E. O'Brien, E. K. McGuire, B. M. Sanchez, G. S. Duesberg, N. McEvoy, T. J. Pennycook, C. Downing, A. Crossley, V. Nicolosi, J. N. Coleman, *Nat. Mater.* **2014**, *13*, 624.

[6] a) C. Zhang, M. P. Kremer, A. Seral-Ascaso, S.-H. Park, N. McEvoy, B. Anasori, Y. Gogotsi, V. Nicolosi, *Adv. Funct. Mater.* **2018**, *28*, 1705506; b) P. He, J. Cao, H. Ding, C. Liu, J. Neilson, Z. Li, I. A. Kinloch, B. Derby, *ACS Appl. Mater. Interfaces* **2019**, *11*, 32225; c) T. Carey, S. Cacovich, G. Divitini, J. Ren, A. Mansouri, J. M. Kim, C. Wang, C. Ducati, R. Sordan, F. Torrisi, *Nat. Commun.* **2017**, *8*, 1202; d) J. Ren, C. Wang, X. Zhang, T. Carey, K. Chen, Y. Yin, F. Torrisi, *Carbon* **2017**, *111*, 622.

[7] V. Nicolosi, M. Chhowalla, M. G. Kanatzidis, M. S. Strano, J. N. Coleman, *Science* **2013**, *340*, 1226419.

[8] A. G. Kelly, D. O'Suilleabhain, C. Gabbett, J. N. Coleman, *Nat. Rev. Mater.* **2022**, *7*, 217.

[9] a) S. Barwich, J. Medeiros de Araújo, A. Rafferty, C. Gomes da Rocha, M. S. Ferreira, J. N. Coleman, *Carbon* **2021**, *171*, 306; b) C. Gabbett, L. Doolan, K. Synnatschke, L. Gambini, E. Coleman, A. G. Kelly, S. Liu, E. Caffrey, J. Munuera, C. Murphy, *arXiv preprint arXiv:2301.11046* **2023**, https://doi.org/10.21203/rs.3.rs-2723977/v1.

[10] a) H. M. Jaeger, S. R. Nagel, R. P. Behringer, *Rev. Mod. Phys.* **1996**, *68*, 1259; b) E. T. Bowman, K. Soga, *Soils Foundations* **2003**, *43*, 107; c) G. R. McDowell, J. J. Khan, *Granular Matter* **2003**, *5*, 115; d) A. Gnoli, L. de Arcangelis, F. Giacco, E. Lippiello, M. P. Ciamarra, A. Puglisi, A. Sarracino, *Phys. Rev. Lett.* **2018**, *120*, 138001.

[11] a) T. Y. Tsui, G. M. Pharr, *J. Mater. Res.* **1999**, *14*, 292; b) N. G. Chechenin, J. Bøttiger, J. P. Krog, *Thin Solid Films* **1995**, *261*, 219; c) B. Jönsson, S. Hogmark, *Thin Solid Films* **1984**, *114*, 257; d) R. Saha, W. D. Nix, *Acta Mater.* **2002**, *50*, 23.

[12] a) A. P. Philipse, *Langmuir* **1996**, *12*, 1127; b) M. Nardin, E. Papirer, J. Schultz, *Powder Technol.* **1985**, *44*, 131.

[13] a) M. J. Solomon, P. T. Spicer, *Soft Matter* **2010**, *6*, 1391; b) T. Yamamoto, M. Yoshida, *Langmuir* **2012**, *28*, 8463; c) G. Katgert, M. E. Möbius, M. van Hecke, *Phys. Rev. Lett.* **2008**, *101*, 058301.

[14] M. Macaulay, P. Rognon, *Soft Matter* **2021**, *17*, 165.

[15] a) J. A. Baimova, B. Liu, S. V. Dmitriev, K. Zhou, *J. Phys. D: Appl. Phys.* **2015**, *48*, 095302; b) Y. A. Baimova, R. T. Murzaev, S. V. Dmitriev, *Phys. Solid State* **2014**, *56*, 2010.

[16] A. D. Sinnott, O. Brazil, G. L. Cross, *Front. Mater.* **2022**, *9*, 906204.

[17] G. L. W. Cross, B. S. O'Connell, J. B. Pethica, H. Rowland, W. P. King, *Rev. Sci. Instrum.* **2008**, *79*, 013904.

[18] a) J. N. Coleman, *Acc. Chem. Res.* **2013**, *46*, 14; b) M. Lotya, Y. Hernandez, P. J. King, R. J. Smith, V. Nicolosi, L. S. Karlsson, F. M. Blighe, S. De, Z. Wang, I. T. McGovern, G. S. Duesberg, J. N. Coleman, *J. Am. Chem. Soc.* **2009**, *131*, 3611.

[19] a) S. Ippolito, A. G. Kelly, R. Furlan de Oliveira, M.-A. Stoeckel, D. Iglesias, A. Roy, C. Downing, Z. Bian, L. Lombardi, Y. A. Samad, V. Nicolosi, A. C. Ferrari, J. N. Coleman, P. Samorì, *Nat. Nanotechnol.* **2021**, *16*, 592; b) S. Ippolito, F. Urban, W. Zheng, O. Mazzarisi, C. Valentini, A. G. Kelly, S. M. Gali, M. Bonn, D. Beljonne, F. Corberi, J. N. Coleman, H. I. Wang, P. Samorì, *Adv. Mater.* **2023**, *35*, 2211157.

[20] a) W.-G. Jiang, J.-J. Su, X.-Q. Feng, *Eng. Fract. Mech.* **2008**, *75*, 4965; b) Y. Xia, M. Bigerelle, J. Marteau, P.-E. Mazeran, S. Bouvier, A. Iost, *Scanning* **2014**, *36*, 134; c) S. A. Epshtein, F. M. Borodich, S. J. Bull, *Appl. Phys. A* **2015**, *119*, 325; d) Y. Yang, J. F. Zeng, J. C. Ye, J. Lu, *Appl. Phys. Lett.* **2010**, *97*, 261905.

[21] O. Brazil, J. P. de Silva, M. Chowdhury, H. Yoon, G. B. McKenna, W. C. Oliver, J. Kilpatrick, J. B. Pethica, G. L. W. Cross, *J. Mater. Res.* **2020**, *35*, 644.

[22] O. Brazil, J. P. de Silva, J. B. Pethica, G. L. W. Cross, *Philos. Mag.* **2021**, *101*, 1327.

[23] O. Brazil, J. P. de Silva, M. Chowdhury, H. Yoon, G. B. McKenna, W. C. Oliver, J. Kilpatrick, J. B. Pethica, G. L. Cross, *J. Mater. Res.* **2020**, *35*, 644.

[24] G. L. W. Cross, J. B. Pethica, H. Rowland, W. P. King, *Rev. Sci. Instrum.* **2008**, *79*, 013904.

[25] A. D. Sinnott, A. Kelly, C. Gabbett, M. Mobius, J. Coleman, G. LW, Trinity College Dublin, TARA preprint **2023**, https://doi.org/10.25546/102970.

[26] J. D. Eshelby, R. E. Peierls, *Proc. R. Soc. London, Ser. A* **1997**, *252*, 561.

[27] M. Nejati, M. L. T. Dambly, M. O. Saar, *J. Rock Mech. Geotech. Eng.* **2019**, *11*, 1166.

[28] T. Uhlířová, W. Pabst, *J. Am. Ceram. Soc.* **2020**, *103*, 6961.

[29] M. P. Lutz, R. W. Zimmerman, *Math. Mech. Solids* **2021**, *26*, 1191.

[30] C. M. Sayers, *Geophys. Prospect.* **2013**, *61*, 416.

[31] a) J. Brandrup, E. H. Immergut, E. A. Grulke, A. Abe, D. R. Bloch, *Polymer Handbook*, Wiley, New York **1999**; b) J. E. Mark, *Physical Properties of Polymers Handbook*, Springer, New York **2007**.

[32] a) A. J. Wood, *Physica A* **2002**, *313*, 83; b) B. A. DiDonna, T. A. Witten, *Phys. Rev. Lett.* **2001**, *87*, 206105.

[33] T. A. Witten, *Rev. Mod. Phys.* **2007**, *79*, 643.

[34] E. Han, J. Yu, E. Annevelink, J. Son, D. A. Kang, K. Watanabe, T. Taniguchi, E. Ertekin, P. Y. Huang, A. M. van der Zande, *Nat. Mater.* **2020**, *19*, 305.

[35] C. Backes, D. Campi, B. M. Szydlowska, K. Synnatschke, E. Ojala, F. Rashvand, A. Harvey, A. Griffin, Z. Sofer, N. Marzari, J. N. Coleman, D. D. O'Regan, *ACS Nano* **2019**, *13*, 7050.

[36] S. Barwich, M. E. Möbius, *Soft Matter* **2022**, *18*, 8223.

[37] S. Xiong, G. Cao, *Nanotechnology* **2016**, *27*, 105701.

[38] a) M. J. Large, S. P. Ogilvie, A. Amorim Graf, P. J. Lynch, M. A. O'Mara, T. Waters, I. Jurewicz, J. P. Salvage, A. B. Dalton, *Adv. Mater. Technol.* **2020**, *5*, 200284; b) X. Huang, T. Leng, X. Zhang, J. C. Chen, K. H. Chang, A. K. Geim, K. S. Novoselov, Z. Hu, *Appl. Phys. Lett.* **2015**, *106*, 203105.

[39] a) X. Chen, C. Yi, C. Ke, *Appl. Phys. Lett.* **2015**, *106*, 101907; b) J. W. Jiang, *Nanotechnology* **2014**, *25*, 355402.

[40] S. M. A. Kazimi, *Solid Mechanics*, Tata McGraw-Hill, New York, **2001**.

[41] E. D. Cubuk, R. Ivancic, S. S. Schoenholz, D. Strickland, A. Basu, Z. Davidson, J. Fontaine, J. L. Hor, Y.-R. Huang, Y. Jiang, *Science* **2017**, *358*, 1033.

[42] a) O. Nakada, *J. Phys. Soc. Jpn.* **1955**, *10*, 804; b) K. L. Johnson, *Contact Mechanics*, Cambridge University Press, Cambridge **1985**; c) E. G. Herbert, W. C. Oliver, A. Lumsdaine, G. M. Pharr, *J. Mater. Res.* **2009**, *24*, 626.

[43] a) W.-L. Yang, S.-S. Hsiau, *Chem. Eng. Sci.* **2006**, *61*, 6085; b) F. D. Cruz, F. Chevoir, D. Bonn, P. Coussot, *Phys. Rev. E* **2002**, *66*, 051305; c) M. Rauter, T. Barker, W. Fellin, *Comput. Geotech.* **2020**, *122*, 103492; d) M. L. Sweat, A. S. Parker, S. P. Beaudoin, *Powder Technol.* **2016**, *302*, 480.

[44] M. T. Shaw, W. J. MacKnight, *Introduction to Polymer Viscoelasticity*, John Wiley & Sons, New Jersey **2018**.

[45] S. Cottrino, P. Viviès, D. Fabrègue, E. Maire, *Acta Mater.* **2014**, *81*, 98.
[46] D. J. Plazek, V. M. O'Rourke, *J. Polym. Sci., Polym. Phys. Ed.* **1971**, *9*, 209.
[47] R. Edgeworth, B. J. Dalton, T. Parnell, *Eur. J. Phys.* **1984**, *5*, 198.
[48] Z. Liu, J. Z. Liu, Y. Cheng, Z. Li, L. Wang, Q. Zheng, *Phys. Rev. B* **2012**, *85*, 205418.
[49] C. S. Boland, U. Khan, G. Ryan, S. Barwich, R. Charifou, A. Harvey, C. Backes, Z. Li, M. S. Ferreira, M. E. Möbius, R. J. Young, J. N. Coleman, *Science* **2016**, *354*, 1257.
[50] a) J. Torres, Y. Zhu, P. Liu, S. C. Lim, M. Yun, *Phys. Status Solidi A* **2018**, *215*, 1700512; b) S. Chen, Q. Bai, S. Wang, H. Wang, W. Guo, Y. Dou, *ACS Appl. Nano Mater.* **2023**, *6*, 2942.